Nonlinear formulation of the bulk surface stress over breaking waves: feedback mechanisms from air-flow separation

James Mueller (jmueller@udel.edu) and Fabrice Veron (fveron@udel.edu)
College of Marine and Earth Studies, University of Delaware,
112C Robinson Hall, Newark, DE 19716, U.S.A.

Abstract. Historically, our understanding of the air-sea surface stress has been derived from engineering studies of turbulent flows over flat solid surfaces, and more recently, over rigid complex geometries. Over the ocean however, the presence of a free, deformable, moving surface gives rise to a more complicated drag formulation. In fact, within the constant stress atmospheric turbulent boundary layer over the ocean, the total air-sea stress not only includes the traditional turbulent and viscous components but also incorporates surface wave effects such as wave growth or decay, air-flow separation, and surface separation in the form of sea spray droplets. Because each individual stress component depends on and alters the sea state, a simple linear addition of all stress components is too simplistic. In this paper we present a model of the air-sea surface stress which incorporates air-flow separation and its effects on the other stress components such as a reduction of the the surface viscous stress in the separated region as suggested by recent measurements. Naturally, the inclusion of these effects leads to a nonlinear stress formulation. This model reproduces the observed features of the drag coefficient from low to high wind speeds despite extrapolating empirical wave spectra and breaking wave statistics beyond known limits. The model shows the saturation of the drag coefficient at high wind speeds for both field and laboratory fetches, suggesting that air-flow separation over ocean waves and its accompanying effects may play a significant role in the driving physics of the air-sea stress, at least at high wind speeds.

Keywords: Sea drag, Breaking wind waves, Sea roughness, Wave boundary layer, Air-flow separation

1. Introduction

Accurate evaluation and prediction of the stress at the surface of the ocean is critical to a large range of problems including air-sea heat, moisture, and gas exchanges because turbulent diffusivity generally dominates its molecular counterpart by orders of magnitude, and thus, is the primary mechanism for transport. Unfortunately, the range of scales involved renders direct numerical simulation inadequate for models of these air-sea processes. Furthermore, high resolution data are sparse, and detailed experiments are unsuitable for routine field observations. Therefore, most applications require that the surface stress be derived from readily obtained and resolved variables. For flow over a smooth, flat plate, upon which boundary layer turbulence theory is derived, this approach is quite successful because the stress in the vicinity of the surface can be considered to be constant, resulting in the well-known "law of the wall." Succinctly, the law of the wall identifies three distinct layers: the viscous sublayer, where molecular stresses dominate, a log layer, where the turbulent stresses dominate, and a defect layer. Except in the defect layer, the constant stress layer assumption lead to self similar functions for the velocity profile in the form of the classical log-linear profiles. Unlike air-flow over flat surfaces, individual stress components for the marine boundary layer are not well resolved, and their interactions are even more obscure. The complicating factor for the oceanic case is the presence of a free surface at the boundary. As the wind blows over the ocean, waves form, grow, interact with each other, and eventually break. In addition to the stress from the viscous boundary effects and turbulence, there is also stress due to the form of the waves (e.g. Janssen 1989; Edson and Fairall, 1998; Hare et al., 1997; Belcher and Hunt, 1993; Makin et al., 1995). Therefore, the stress at the surface is highly dependent on the sea-state. For the purpose of this paper, we split the stress from the waves (form drag) into the two main components: wave-induced and air-flow separation. For purely wind-wave seas, the wave-induced stress component is the momentum flux into the ocean, which creates, feeds, and maintains the waves. Air-flow separation stress occurs when the waves become too steep for the air to follow the surface.

In recent years, several authors have used air-flow separation to explain both an increase and a decrease in the drag coefficient relative to extrapolated, bulk values at high wind speeds where data are sparse. On the one hand, field and laboratory data suggest that the drag coefficient peaks when the $10-m$ wind speed reaches roughly 34 ms^{-1} and afterwards decreases (Powell et al., 2003; Donelan et al., 2004). On the other hand, previous numerical models of surface stress that include air-flow separation predict even higher values for the drag coefficient than those extrapolated from bulk parameterizations (Kudryavtsev and Makin, 2001; Makin and Kudryavtsev, 2002). More recently, a first attempt, which explicitly models air-flow separation and its resulting feedback, has reproduced the saturation of the drag coefficient at laboratory fetches (Kudryavtsev and Makin, 2007; hereafter KM07). The objective of this paper is to formulate an explanation for the observed behavior of the drag coefficient in the presence of air-flow separation for both laboratory and field fetches. Our model includes effects from air-flow separation yielding both a novel, non-linear formulation and fundamentally different results from that previously reported.

2. The atmospheric boundary layer

Using the bulk formulae, the turbulent momentum flux is expressed as:

$$-\overline{u'w'} = u_*^2 = \frac{\tau}{\rho_a} = C_D\left(U_{10} - U_0\right)^2. \tag{1}$$

The primes indicate turbulent quantities (away from the influence of viscosity and waves) and the overbars represent ensemble averages. The air-side friction velocity and mean velocity are noted u_* and U, respectively; the density of air is noted as ρ_a. The quantities C_D and τ are the bulk transfer coefficient for momentum, i.e. the drag coefficient, and the surface stress, respectively. Finally, a subscript 0 indicates the value taken at the interface and a subscript 10 indicates the $10-m$ height value. When the flow is neutrally buoyant, the velocity profile away from the boundary, where viscous effects are negligible, can then be evaluated from well-known law of the wall:

$$U(z) - U_0 = \frac{u_*}{\kappa} ln\left(\frac{z+\delta}{z_0}\right) \tag{2}$$

where κ is the von Karman constant (~ 0.4); z_0 is the roughness length, which parameterizes the influence of the roughness elements at the surface on the kinematics and dynamics of the flow, and $\delta = \alpha z_0$, usually with $\alpha = 1$, is introduced such that the profile is not singular at the surface ($z = 0$).

In smooth flows over a flat plate, a viscous sublayer forms near the surface in which the velocity profile is linear rather than logarithmic. In wall coordinates, $z^+ = zu_*/\nu$ and $U^+ = U/u_*$, the profile is also self-similar linear, $U^+ = z^+$. The van Driest damping function (van Driest, 1956) approximates both the near-wall linear sublayer and the smooth transition to the log layer:

$$U^+ = A_1\left(1 - e^{\frac{-z^+}{A_1}}\right), \tag{3}$$

where A_1 is a constant, typically on the order of O(10) for smooth flow (corresponding to the height of the viscous sublayer). The presence of waves causes the flow to depart from smooth flow and become transitionally rough for most wind speeds. Therefore, the moving, wavy bottom boundary needs to be considered.

3. Parameterization

3.1. Boundary conditions and profile

In the model presented here, once U_{10} is specified, the form for the velocity profile is determined using a hybrid of the van Driest damping function and the standard logarithmic profile described above. In fact, the profile is simply the summation of the two layers with the logarithmic layer exponentially damped in the near-wall region, as follows:

$$\begin{aligned} U(z) - U_0 \;=\; & A_1 u_{*_v} \left(1 - e^{\frac{-z^+}{A_1}}\right) \frac{u_{*_v}}{u_*} \\ & + \frac{u_*}{\kappa} ln\left(\frac{z+\delta}{\delta}\right)\left(1 - e^{\frac{-z^+}{A_1}}\right), \end{aligned} \tag{4}$$

where $\rho_a u_{*_v}^2$ represents the viscous component of the surface stress, and $A_1 = 10$ is the height of the viscous sublayer in wall coordinates. Finally, the surface drift is set to $U_0 = 15.2 u_{*_v} \sqrt{\frac{\rho_a}{\rho_w}} = 0.53 u_{*_v}$ (Wu, 1983), where ρ_w is the density of the surface water and $\rho_a u_{*_v}^2$ is the viscous component of the surface stress. The profile given in equation 4 offers a continuous (and second-order differentiable) formulation that smoothly connects the viscous and log layers. The modification of the van Driest component accounts for the roughness of the flow and converges to the standard definition given in equation 3 for the smooth flow limit, i.e. the limit $z^+ \to 0$ yields $U^+ = z^+ \frac{u_{*_v}^2}{u_*^2}$, which reduces to $U^+ = z^+$ in the smooth flow limit where the surface stress is entirely due to viscosity. Accordingly, the viscous stress at the surface is $\nu \frac{dU}{dz}|_{z=0} = u_{*_v}^2$. Outside the viscous sublayer, the profile converges to the standard log layer:

$$U(z) - U_0 = \frac{u_*}{\kappa} ln\left(\frac{z + \alpha z_0}{z_0}\right), \tag{5}$$

with

$$\alpha = e^{\frac{\kappa A_1 u_{*_v}^2}{u_*^2}}. \tag{6}$$

The coefficient, α, merely shifts the profile near the surface in order to match the linear sublayer such that at the limit $z^+ \to \infty$, the profile converges to:

$$U(z) - U_0 = \frac{u_*}{\kappa} ln\left(\frac{z}{z_0}\right). \tag{7}$$

As the air-flow tends toward the fully rough regime, the slope of the viscous sublayer velocity profile, in wall coordinates, decreases relative to the smooth case. Consequently, the viscous sublayer only plays a dominant role at low winds speeds, while the form drag dominates the stress for moderate to high wind speeds. The only remaining variables yet to be defined are the two friction velocities, u_* and u_{*_v}. Their parameterization is the subject of the next section.

3.2. SURFACE WAVES

In the present model, the bottom boundary is a surface wind-wave field of deep water, gravity and capillary wave modes. The wavenumber range is specified with an implicit lower limit, $k_{min} = 0.07^2 g/u_*^2$ (Plant, 1982) where $g \approx 9.81$ is the gravitational acceleration constant. The spectrum follows an empirical, directional wavenumber spectrum, $\Psi(k,\theta)$ (Elfouhaily et al., 1997), where k and θ are respectively the wavenumber and angle between the wind and wave propagation directions. This empirical wave spectrum captures the observed fetch dependent nature of both the high wave number (Cox and Munk, 1954; Jähne and Riemer, 1990; Hara et al., 1994) and low wave number (Phillips, 1985; Kitaigorodskii, 1973) regimes. Therefore, the spectrum is not only a function of the friction velocity, u_*, but also the inverse wave age, Ω, which is a function of normalized fetch, $X^* = Xg/U_{10}^2$:

$$\Omega = U_{10}/c_p = 0.84 \tanh\left((X^*/X_0)^{0.4} \right)^{-0.75}, \tag{8}$$

where X is the fetch, c_p is the peak wave phase speed and $X_0 = 2.2 \times 10^4$ is an empirical constant (Elfouhaily et al., 1997).

3.3. SURFACE STRESS AND AIR-FLOW SEPARATION

Banner and Peirson (1998) found that the surface stress in the smooth flow limit is the upper limit for the tangential stress at the surface in the laboratory. Intuitively, and in the absence of contradicting data, this result seems reasonable for extension to field cases as a first approximation. In the model, the viscous surface stress without accounting for the effect of air-flow separation, $\tau_\nu^0 = \rho_a \left(u_{*_\nu}^0\right)^2$, is approximated by the equivalent stress in the smooth flow limit. Here, the superscript 0 refers to values that do not consider the feedback effects of the air-flow separation. By prescribing the 10-m wind speed, profile form (equation 4), and roughness length for smooth flow, i.e. $z_0 = 0.11 \frac{\nu}{u_*^0}$, the equivalent stress for smooth flow can be found.

For the total stress at the surface in the presence of air-flow separation, the individual stress components (viscous, wave-induced, and separation) are converged upon and summated using:

$$\tau|_{z=0} = \rho_a u_*^2 = f_1 \tau_\nu^0 + f_2 \tau_w^0 + f_3 \tau_s^0, \tag{9}$$

where τ_w^0 and τ_s^0 are the surface wave-induced and separation stresses (without air-flow separation feedback effects), respectively. The parameters, f_1, f_2, and f_3 account for the effects of airflow separation on these stresses and will be discussed shortly. The wave-induced stress, τ_w^0, is found by the integration of the contributions from all waves:

$$\tau_w^0|_{z=0} = \rho_w \int_{k_{min}}^{\infty} \int_{-\frac{\pi}{2}}^{\frac{\pi}{2}} \beta(k,\ \theta)\omega k \Psi(k,\ \theta) \cos\theta d\theta dk, \tag{10}$$

where $\beta(k,\ \theta)$ is the wave growth rate, and ω is the wave angular frequency. Except for the use of the hybrid velocity profile (equation 4), the separation stress, τ_s^0, is modelled as in Kudryavtsev and Makin (2001); their equation (14) with minor modification can be written as:

$$\tau_s^0|_{z=0} = \rho_a \varepsilon_b \gamma \int_0^{20\pi} \int_{-\pi}^{\pi} u_s(k)^2 \cos\theta \Lambda(k,\ \theta) d\theta dk, \tag{11}$$

where ε_b is the characteristic slope of the breaking wave, γ is an empirical constant relating the pressure drop due to the separation region to the velocity of the air-flow, and finally $u_s(k) = U(\varepsilon_b/k)\cos\theta -$

$c(k)$ is the wind speed at height, $z = \varepsilon_b/k$, in reference to the wave phase speed $c(k)$. The upper wavenumber limit for contribution to the separation stress is taken to be 20π as Makin and Kudryavtsev (2002). The effect of air-flow separation on each of these stress components must now be considered.

We assume that air-flow separation only occurs in the presence of a wave breaking event. Therefore, the occurrence of breaking waves is the foundation for the air flow separation stress and feedback effects. The probability of a wave crest breaking within the wavenumber range (**k**, **k**+d**k**) is:

$$P_{br}(k,\ \theta) = \frac{2\pi}{k}\tilde{L}, \tag{12}$$

where $\tilde{L} = \Lambda(k,\ \theta)kd\theta dk$ is the total length of breaking wave crests per unit area of ocean surface for waves within the wavenumber range (**k**, **k**+d**k**). When the spectral dissipation due to breaking is assumed to be roughly equal to the spectral wind energy input (Kudryavtsev and Makin, 2001), $\tilde{L}$ can be approximated as:

$$\Lambda(k,\ \theta)kd\theta dk = \frac{\beta(k,\ \theta)k^4\Psi(k,\ \theta)d\theta dk}{\omega b}, \tag{13}$$

where b is the normalized dissipation rate of breaking waves.

For a monochromatic wave field, the fraction of sea surface area exposed to air-flow separation over a breaking wave would be:

$$\tilde{A} = LP_{br}, \tag{14}$$

where L is the length of the separation region normalized by the wavelength which we will discuss later. In the presence of multiple wave modes, some separated regions may overlap. For example, in the case where a large, dominant wave crest breaks and the separated region extends such that it covers a fraction of the surface containing subsequent smaller breaking waves, then these smaller waves could not induce separation that would impact additional sea surface area. Therefore, noting that the fraction of area that is not affected by air flow separation per unit wavenumber is $Q(k) = 1 - \int_\theta LP_{br}(k,\ \theta)$, the fraction of area per unit wavenumber exposed to separation is the fractional probability of unaffected area from all longer waves multiplied by the fraction of affected area of the corresponding monochromatic wave:

$$\tilde{A}(k) = \prod_{k'<k}\left[Q(k')\right] \times \int_\theta LP_{br}(k,\ \theta). \tag{15}$$

The total fraction of area exposed to air-flow separation is the area over all wavenumbers, i.e. $A = \int_k \tilde{A}(k)$. With the fraction of sea surface exposed to air-flow separation, the parameters f_1, f_2, and f_3 accounting for the effect of separation on the multiple stress components follow naturally:

$$f_1 = 1 - A, \tag{16}$$

$$f_2(k) = 1 - \int_0^k \tilde{A}(k'), \tag{17}$$

$$f_3(k) = \frac{\tilde{A}(k)}{\int_\theta P_{br}(k,\ \theta)}. \tag{18}$$

The first parameter f_1 simply accounts for the reduction of viscous stress due to the total sea surface area exposed to air-flow separation. Physically, this means that the viscous stress at the surface vanishes within the separation bubble. This is consistent with recent laboratory experiments (Reul, 1998; Veron et al., 2007) that show the surface viscous stress is vastly reduced in the region of air-flow separation. The second parameter f_2 assumes that there is a cascades from all longer waves represented as a cumulative sum of the fraction of sea surface area exposed to separation (Kudryavtsev and Makin, 2007). Finally, the third parameter f_3 adjusts the separation stress from a breaking wave statistics to the modified air-flow separation statistics. In other words, the probability of an air-flow separation event is less than or equal to that of a breaking wave event because multiple breaking waves could have overlapped separation regions. Accounting for feedback, the effective viscous, wave-induced, and separation stresses respectively become $\tau_\nu = f_1\tau_\nu^0$, $\tau_w = \int_k f_2 d\tau_w^0$, and $\tau_s = \int_k f_3 d\tau_s^0$, and the total stress is now:

$$\tau|_{z=0} = \tau_\nu + \tau_w + \tau_s, \tag{19}$$

where $d\tau_w^0$ and $d\tau_s^0$ are respectively the spectral densities of wave-induced and separation stresses without air-flow separation effects.

If the wave growth parameter is conceptualized as the rate of energy transferred from the wind to waves normalized by wave energy, then the presence of multiple wave modes intuitively impacts the energy transfer. The dependence of the growth rate on the local turbulent stress within the inner layer stems from the theory of Belcher and Hunt (1993). Essentially, longer waves shelter shorter waves, resulting in reduced local turbulent stress for the wave boundary layer of shorter waves whose top is still within the wave boundary layer of the longer waves (Makin and Kudryavtsev, 1999). We follow the assumptions made by Hara and Belcher (2002) such that the growth rate depends upon the local turbulent stress available for each wave mode, and the stress induced by each wave mode is constant within the wave boundary layer and zero outside of it. Approximating the wave-induced stress for each wave mode as a step function simplifies the parameterization considerably and does not seem to render drastically different drag coefficients compared to more complex decay functions (Makin et al., 1995). Therefore, within the constant stress layer, the wave-induced stress discontinuously becomes turbulent stress outside the inner region. We also assume that the separation stress from all wave modes is part of the turbulent stress throughout the constant stress layer. Consequently, the maximum turbulent stress available for each wave mode is the summation of the total viscous and separation stresses and the wave-induced stress of all smaller waves. In other words, for each wave mode the stress carried by all shorter wave modes contributes to the stress in the wave growth parameter such that:

$$\beta(k,\ \theta) = \frac{C_b(k)\omega(k)}{\rho_a c(k)^2}\left(\tau_\nu + \tau_s + \int_k^\infty d\tau_w(k')\right), \tag{20}$$

where $C_b(k)$ is in the range 0.04 ± 0.02 (Plant, 1982) and $d\tau_w(k')$ is the spectral wave-induced stress. To limit wave growth to the wind-wave regime, the following smooth cutoff for $C_b(k)$ is used:

$$C_b(k) = B - B\tanh\left(\frac{c(k)}{2u_*} - 1.8\pi\right), \tag{21}$$

where B is a constant taken to be 0.02. Thus, for young waves, the value for C_b is 0.04, which corresponds to Plant's mean value. With increasing wave age, the constant transitions smoothly to zero at the wind-wave limit and remains zero for all older waves, which in effect prohibits negative wave growth (i.e. the transfer of momentum from the waves beyond the wind-wave limit to the air).

Three of the empirically derived parameters used in modelling both the separation stress and resulting feedback, namely the breaking wave slope (ε_b), the normalized dissipation rate of the breaking wave (b), and the normalized length of the separation bubble (L), remain to be parametrized. The slope of breaking waves can be less than 0.2 on the low end (Wu and Yao, 2004) and greater than 0.6 on the high end (Duncan, 1981). For the dominant waves, the significant slope is often used as the characteristic breaking wave slope:

$$\varepsilon = \frac{H_p k_p}{2} = \frac{4k_p}{2}\left[\int_{0.7f_p}^{1.3f_p} \Psi(f)df\right]^{\frac{1}{2}}, \tag{22}$$

where the subscript p denotes peak wave properties, f is the wave frequency, and H_p is the significant wave height of the peak waves. Here, we employ a slightly different, yet equivalent characteristic breaking slope as that above, and offer a unified form for the dominant and equilibrium regimes. Indeed, for the dominant waves, the significant slope scales (by a factor of 2) with the root-mean-square slope of the dominant waves. Thus, for both regimes, dominant and equilibrium, we can take the characteristic breaking wave slope as:

$$\varepsilon_b(k) = 2\left[\int S(k)dk\right]^{\frac{1}{2}}, \tag{23}$$

where $S(k) = \int_{-\pi}^{\pi} k^2\Psi(k,\ \theta)kd\theta$ is the slope spectrum. The limits of integration for the dominant waves are the corresponding wavenumbers to the frequency limits given for the significant slope calculation, while the limits for the equilibrium range include all wavenumbers above the dominant waves up to the cutoff for separation ($k = 20\pi$). Presumably, breaking wave events with small slopes are more likely to be a spilling wave, while the breaking events at greater slopes are more likely to be a plunging wave.

The normalized dissipation rate for breaking waves, b has been found to span a wide range of values from 10^{-4} to 10^{-1} (e.g. Duncan, 1981; Melville, 1994; Phillips et al., 2001; Drazen, 2006; Banner and Peirson, 2007), and is thought to depend on the slope of breaking waves (Melville, 1994). Indeed, recent work (Drazen, 2006) suggests that the dependence of b on slope is split into the spilling and plunging regimes, respectively:

$$b = \Upsilon \varepsilon_b^{\frac{1}{2}} \tag{24}$$

$$b = \chi \varepsilon_b^{\frac{5}{2}}. \tag{25}$$

The tabulated data from Duncan (1981) suggests that Υ is in the range $0.007 - 0.019$. We take the mean value from Duncan (1981) such that $\Upsilon = 0.013$. Fitting the two regimes at the slope, 0.2, we find the value $\chi = 0.325$. We note here that both values are less than those reported by Drazen (2006) who found $\Upsilon \approx 0.05$ and $\chi \approx 0.849$. Yet, these values are of the same order of magnitude as those of Drazen (2006) and offer a similar and appropriate fit to the available data.

Finally, we need to parametrize the fractional length, L, of the sea surface affected by air-flow separation. Earlier models proposed that $L = 0.75\cos\theta$, where θ is the angle between the wind and wave propagation directions (Csanady, 1985). Kudryavtsev and Makin (2007), assumed that the flow reattached at the following crest, i.e. $L = 1$, in the case of copropagating wind and waves. This certainly is the upper bound and realistically, the length of the separated region is less than the wavelength. In both cases, the length of the air-flow separation region normalized by wavelength is a constant fraction of the wavelength. The length of the area exposed to the separation bubble, however, presumably depends upon the slope of the wave (Reul et al., 2007). Thus, we propose that

$$L(k) = \left(\varepsilon_b(k)^{\frac{1}{2}} + \frac{1}{4}\right)\cos\theta. \tag{26}$$

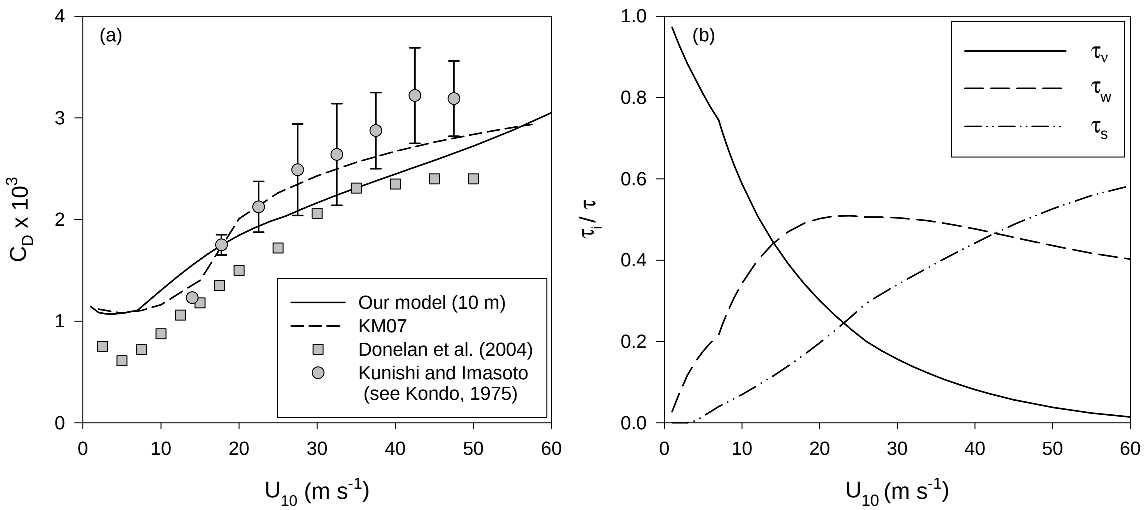

Figure 1. (a) Drag coefficient as a function of wind speed for a 10 *m* fetch (solid line) along with the experimental data of Kunishi and Imasoto (circles) and Donelan et al. (2004) (squares). Model results from KM07 (dashed line) are also included. (b) Fraction of the viscous (line), wave-induced (dashed), and separation (dash-dotted) stresses as a function of wind speed for 10 *m* fetch.

For the range of breaking slopes considered here, L ranges between 0.55 and 1 when the angle between the wave and wind directions is zero. We note, however, that the model results are not very sensitive to the choice of L and are qualitatively similar to the case when $L = 0.75\cos\theta$ for all wave modes.

4. Results

We present here the model output for both laboratory and field fetches and compare the predictions with available data and parameterizations.

4.1. Laboratory comparison

Experimental data at laboratory fetches offer insight not only into the behavior of the drag coefficient at high wind speeds but also into the relative contributions of each stress component at lower wind speeds. This combination of data can be used to assess the role of air-flow separation at extreme conditions. Kunishi and Imasoto (see Kondo, 1975) performed a wind flume experiment at high wind speeds and found that the increase of the drag coefficient with wind speed lessened above $U_{10} = 27\ ms^{-1}$. Furthermore, their data points for the highest two wind speeds suggest that the drag coefficient may actually plateau at high wind speeds. Recently, Donelan et al. (2004) found that the drag coefficient indeed becomes independent of wind speed above $U_{10} = 33\ ms^{-1}$. Figure 1a plots the results from the model for a fetch of 10 *m*. For comparison, we also show the experimental drag coefficients from Kunishi and Imasota (see Kondo, 1975) and Donelan et al. (2004)[1], as well as the model results from KM07. At low wind speeds, our model compares well with that of KM07, but

[1] The data from Donelan et al. (2004) was averaged over the different methods used in their study, as suggested by Mark Donelan - personal communication

both models predict a higher drag coefficient than either experimental data set. At moderate wind speeds, our drag coefficient is substantially higher. This is most likely due to an overestimation of the viscous stress, which will be discussed subsequently. At the higher wind speeds, both models show a trend toward the saturation of the drag coefficient. Figure 1b shows the relative contributions of stress components as a function of wind speed. The maximum fraction of separation stress is roughly 0.6 compared to 0.9 in KM07. It is difficult to directly compare the stress fractions to KM07 since the total stress used to normalize the stress components is different between the models. For example, the fraction of viscous stress would be lower at higher wind speeds, if the total stress were higher. Likewise, if the viscous stress were lower, the fraction of wave-induced and separation stress would also be higher.

We now consider an additional modification of the viscous stress. The laboratory experiments of Jähne and Riemer (1990) suggest that the small gravity-capillary waves near the viscous scale are not completely smeared out of existence. Therefore, the waves, whose inner region, $l_i(k) = \delta/k$, lies completely within the viscous sublayer, i.e. $l_i(k) < 10\nu/u^0_{*\nu}$, must depend on the viscous stress for growth rather than the turbulent stress which is negligible within this layer. Thus, the wave-induced stress for these waves should be subtracted from the viscous stress from the smooth flow limit before accounting for the air-flow separation effects. Although the value for δ is still debated, we take the conservative estimate $\delta = 0.1$, and in conjunction with the conservative estimate for the viscous sublayer height, we find a lower bound of wave growth due to viscous stress. Therefore, the fully modified viscous stress, accounting for both air-flow separation and small wind wave growth becomes:

$$f_\nu = f_1 \left(1 - \frac{\int_{k_\nu}^{\infty} d\tau_w}{\tau_\nu} \right), \tag{27}$$

where $k_\nu = \frac{\delta u^0_{*\nu}}{10\nu}$.

When using f_1 in the model, the only mechanism for the viscous stress to depart from the smooth flow limit is the effects air-flow separation. It is reasonable to believe that the smallest capillary-gravity waves play an important role in altering the viscous stress relative to the smooth flow limit, hence the introduction of f_ν. Figure 2 plots the viscous stress produced by the model versus the total stress along with laboratory data from Banner and Peirson (1998). For comparison, the data from Kukulka and Hara (2005), hereafter KH2005, is also shown. Note that the jaggedness of the results for both our model and KH2005 are due to the data spanning different fetches. We can infer from figure 2 that viscous stress reduction caused by air-flow separation is likely not the only mechanism for the reduction of viscous stress relative to the smooth flow limit. In fact, our model overestimates the viscous stress when using f_1, that is when it accounts only for the separation effects on the viscous stress. The laboratory fetches for these runs are especially small, (2.45 m, 3.10 m, and 4.35 m), so that the smallest waves arguably affect the viscous stress proportionately more than for longer fetches. Nevertheless, when accounting for both the effects due to separation and the wave growth of the smallest waves (by using f_ν), the predicted viscous stress follows the experimental data of Banner and Peirson (1998) quite well. Figure 3 is the extension of figure 2 to higher wind speeds (i.e. total stress) for a 4.35 m fetch. At high wind speeds, both estimates of τ_ν are roughly the same, which is a consequence of more prevalent air-flow separation and of a thinner viscous layer. Because of the latter, the inner regions of few waves are encapsulated by the viscous layer at high wind speeds. In other words, the additional influence of the waves on the viscous stress is significant at either short fetches, such as laboratory conditions, or perhaps in the field under low wind speeds. Consequently, the drag coefficient, when including the effect of the smallest waves on

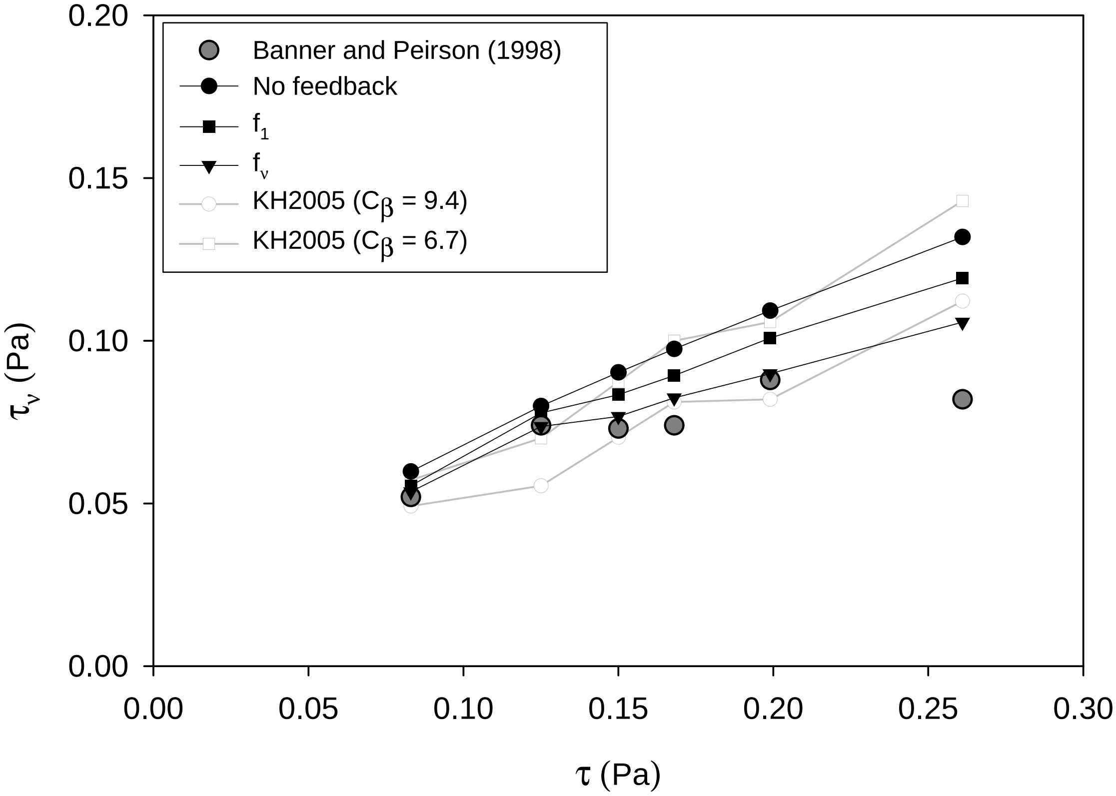

Figure 2. Viscous stress as a function of total stress calculated with no feedback (closed circles), f_1 (closed squares), and f_ν (closed triangles) along with the experimental data of Banner and Peirson (1998) (gray circles) and the Kukulka and Hara (2005) model results with sheltering and infinite wave growth constants, $c_\beta = 9.4$ (open circles) and $c_\beta = 6.7$ (open squares).

the viscous stress, does not substantially change at the lowest and highest wind speeds, but within the wind speed range 10-25 $ms^{-}1$, it is slightly reduced from that shown in figure 1. Therefore, while this additional feedback mechanism perhaps explains the viscous stress at lower wind speeds, it does not explain the flattening drag coefficient at high wind speeds as seen in the experimental data of Donelan et al. (2004).

4.2. Field comparison

Field fetches of a kilometer or more have more practical importance than the laboratory fetches discussed in the previous section. With increasing fetch, the wave field becomes more developed for each particular wind speed, which means that the short, laboratory fetches provide steeper waves and consequently more fractional area affected by air-flow separation. In the ocean, less sea surface area exposed to separation yields less stress due to separation such that the drag coefficient reaches full saturation. Figure 4a shows our predicted drag coefficient for 10 *km* and 100 *km* fetches as well as the infinite limit. For comparison, we also plot the drag of Large and Pond (1981), the data from Taylor and Yelland (2000), and the data from Powell et al. (2003) along with the KM07 model results for a 100 *km* fetch. For the most part, all of the data collapses on the Large and Pond (1981) estimate at lower wind speeds. At moderate wind speeds, the 100 *km* and infinite fetch cases seem

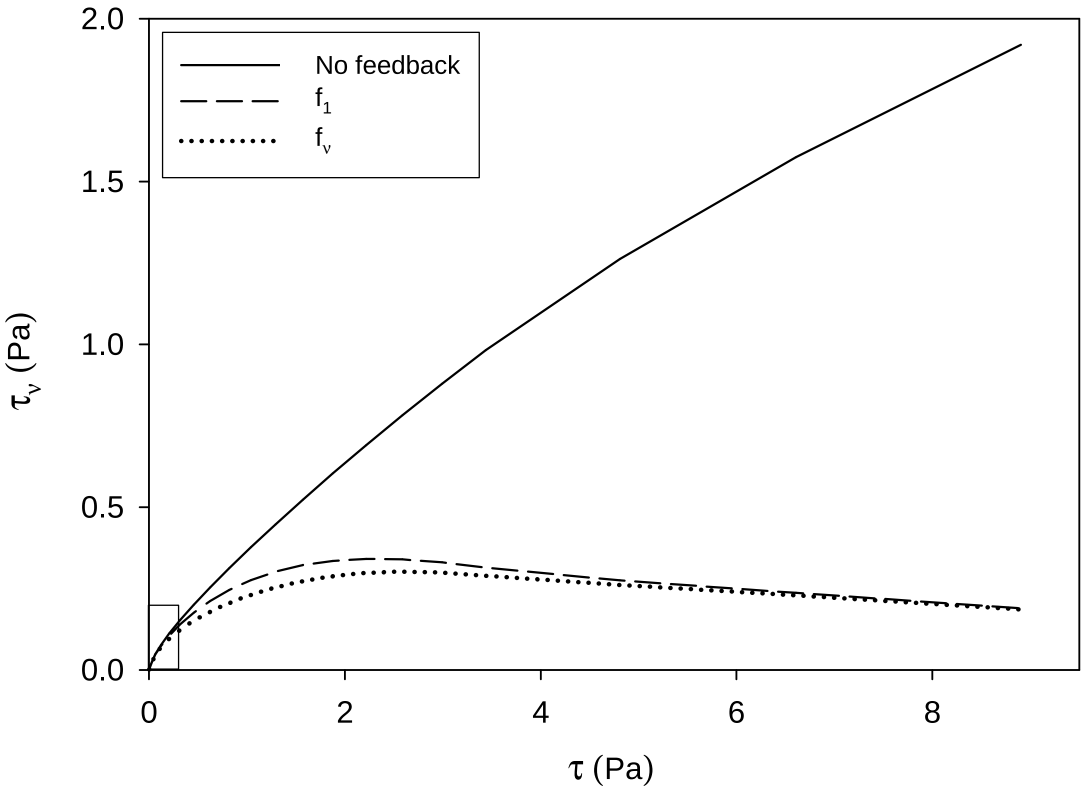

Figure 3. Viscous stress as a function of total stress for a fetch of 4.35 *m* calculated with no feedback (line), f_1 (dashed), and f_ν (dotted) with the range of experimental data from figure 2 denoted by the solid box.

to follow Taylor and Yelland (2000). All of the modelled field drag coefficients plateau somewhere between 35 ms^{-1} and 45 ms^{-1}, even in the infinite fetch limit. The drag coefficient at 10 *km* fetch follows the upper limit of the Powell et al. (2003) data up to 40 ms^{-1} but never decreases as their data suggest. This downward trend with decreasing fetch is consistent with the conclusion of Moon et al. (2004) that the observed reduction of the drag coefficients of Powell et al. (2003) could be due to an extremely limited fetch. Figure 4b plots the fraction of the individual stress components to the total stress for 100 *km* fetch. Compared to the 10 *m* fetch shown in 1b, separation stress does not play as much of a role as it only carries 40 percent of the stress at the highest wind speed. The maximum fraction of separation stress is roughly 0.4 compared to 0.6 in KM07. This is partly a consequence of their model taking the upper bound limit on the length of the separation bubble, thereby maximizing the separation effects in their model. Since there is less separation stress, there is also less fractional area exposed to separation compared to the 10 *m* fetch case, which is easily seen by the greater fraction of viscous stress at the highest wind speeds.

The nondimensional roughness length, or Charnock constant, can further illustrate the different effect of air-flow separation for laboratory and field fetches. Accounting for the smooth flow roughness, the nondimensional roughness due to surface gravity waves is:

$$Z_0^* = \frac{g\left(z_0 - \frac{0.11\nu}{u_{*\nu}}\right)}{u_*^2}. \tag{28}$$

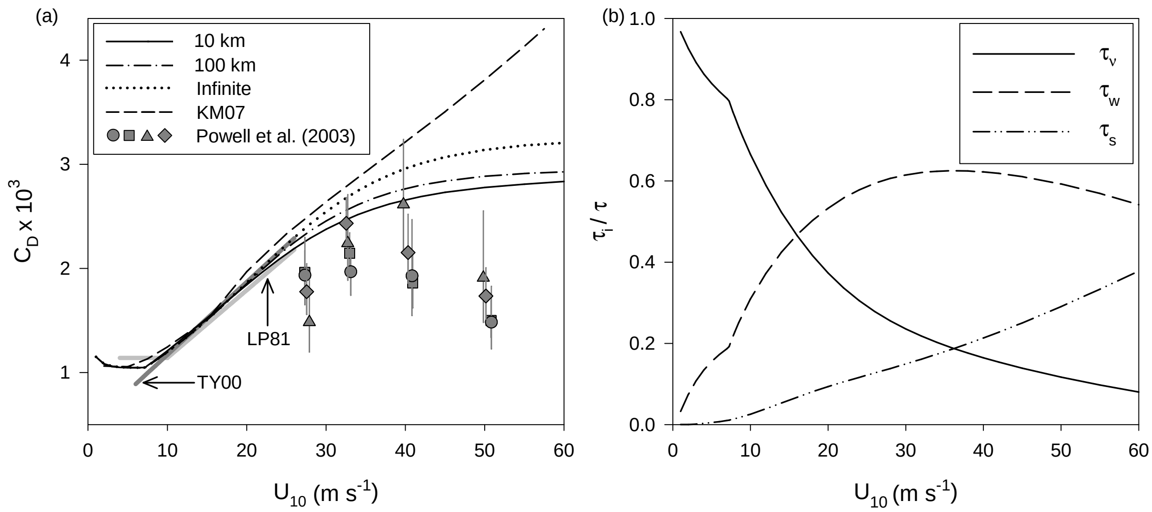

Figure 4. (a) Drag coefficient as a function of wind speed for 10 km (solid), 100 *km* fetch (dash-dotted), and infinite (dotted) fetches along with the experimental data of Large and Pond (1981) (light gray), Taylor and Yelland (2000) (dark gray) and Powell et al. (2003) (gray symbols). Model results from KM07 (dashed line) are also included. (b) Fraction of the viscous (line), wave-induced (dashed), and separation (dash-dotted) stresses as a function of wind speed for a 100 *km* fetch.

Figure 5 shows the nondimensional roughness length for several fetches as a function of wind speed. There is similar behavior for all fetches. The peak roughness, however, shifts to higher wind speeds with increasing fetch, which corresponds to the further development of the wave field with increasing fetch. At low wind speeds, the Charnock coefficient is within the estimates from the San Clemente Ocean Probing Experiment (SCOPE; Edson and Fairall, 1998) and Taylor and Yelland (2000). At high wind speeds, our results are within the Powell et al. (2003) error ranges for wind speeds up to 50 ms^{-1}. It is also interesting that the roughness reaches a minimum at high wind speeds for the 10 *m* fetch. This suggests that the roughness coefficient for field fetches could also reach a minimum at extremely high wind speeds since the behavior of field and lab fetches is similar, but shifted, at the lower wind speeds. If this is indeed the case, air-flow separation effects would be unable to cause the reduction of the drag coefficient at high wind speeds as seen in the data of Powell et al. (2003) because a reduction in the drag coefficient requires a decreasing roughness coefficient.

5. Discussion and conclusion

Although empirical wave spectra and breaking wave statistics are extrapolated beyond known limits, the present model appears to reproduce the observed trend of the drag coefficient better than available models, which also use similar extrapolations. We note however that the spectral description of the wave induced stress and separation stress (equations 10 and 11) rely on the assumption that the wave field can be adequately represented by linear Fourier modes. This assumption might be questionable in the presence of frequent breaking at the higher wind speeds. We also note that the breaking wave statistics used here may very well underestimate actual breaking events, as they rely on equilibrium between input and dissipation, which might not be the case in growing seas, and are based on estimate of the dissipation b which is contentious to this day. This could be especially prevalent in the laboratory. Furthermore, air-flow separation may also occur without any observable

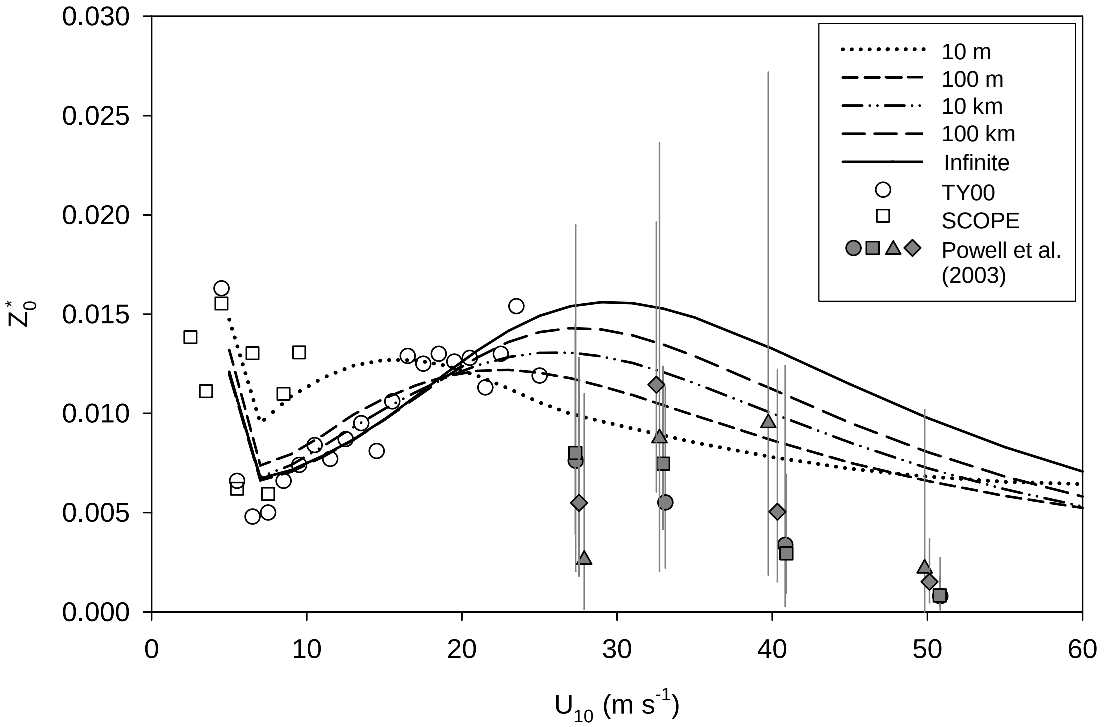

Figure 5. Nondimensional roughness as a function of wind speed for 10 *m* (dotted), 100 *m* (short dashed), 10 *km* (dash-dot-dotted), 100 *km* (long dashed), and infinite (line) fetches along with estimates from various field programs: Taylor and Yelland (2000) (open circles), SCOPE (open squares) and Powell et al. (2003) (gray symbols).

wave breaking, though this remains controversial. In any event, it is likely that air-flow separation is probably more prevalent than its parameterization in both previous studies and this one (Veron et al., 2007).

Nonetheless, this nonlinear stress model, which incorporates air-flow separation effects, can qualitatively reproduce the observed features of the drag coefficient at low and high wind speeds. These results, to the best of our knowledge, are the first, which explicitly includes air-flow separation, and reproduce the complete saturation of the drag coefficient at high wind speeds for field scale fetches. We note however, that the effect of sea spray may also need to be considered at higher wind speeds as recent studies have predicted a significant momentum exchange due to spray (e.g. Andreas, 2004; Makin, 2005; Barenblatt et al., 2005). In fact, if sea spray generation is also a function of wave slope, its contribution to the air-sea momentum flux may in fact further reduce the predicted drag coefficient past 40 ms^{-1} and further improve the agreement between predicted and observed drag at high wind speeds (figure 1 and figure 4). This is the subject of current work and will be reported in subsequent publications. Our results indicate that air-flow separation over ocean waves and the accompanying effects and feedbacks on the multiple stress components may account for a significant portion of the physics that drive the observed trends. Finally, the model results suggest that air-flow separation on a range of scales eventually causes a complete saturation of the drag coefficient regardless of the fetch.

Acknowledgements

We are grateful for the assistance of Tanos 'Tony' Elfouhaily in resolving the wave spectrum model and sincerely regret his untimely passing. We would also like to thank Vladimir Makin for his helpful suggestions and providing the data from KM07. We also would like to thank Mark Donelan, Mark Powell and Tobias Kukulka for providing their data for comparison with the model. This work was supported by ONR grant (N00014-05-1-0609) to Veron.

References

Andreas, EL (2004) Spray Stress Revisited. *J. Phys. Ocean.*, 34:1429–1440

Banner, ML and Peirson, WL (1998) Tangential stress beneath wind-driven air-water interfaces. *J. Fluid Mech.* 364:115–145

Banner, ML and Peirson, WL (2007) Wave breaking onset and strength for two-dimensional deep-water wave groups. *J. Fluid Mech.* 585:93–115

Barenblatt, GI, Chorin, AJ, and Prostokishin, VM (2005) A note concerning the Lighthill "sandwich model" of tropical cyclones. *Proc. Natl. Acad. Sci. USA*, 102:11148–11150

Belcher, SE and Hunt, JCR (1993) Turbulent shear flow over slowly moving waves. *J. Fluid Mech.*, 251:119–148

Cox, CS and Munk, WH (1954) Statistics of the sea surface derived from Sun glitter. *J. Mar. Res.*, 13:198–227

Csanady, GT (1985) Air-sea momentum transfer by means of short-crested wavelets *J. Phys. Ocean.*, 15:1486-1501

Donelan, MA, Haus, BK, Reul, N, Plane, WJ, Stiassnie, M, Grabber, HC, Brown, OB, and Saltzman, ES (2004) On the limiting aerodynamics roughness on the ocean in very strong winds. *Geophys. Res. Let.*, 31:L18306

Drazen, D (2006) Laboratory Studies of Nonlinear and Breaking Surface Waves *Dissertation*, 174 pp., Univ. of Califonia, San Diego

Duncan, JH (1981) An experimental investigation of breaking waves produced by a towed hydrofoil. *Proc. R. Soc. Lond. A*, 377:331-348

Edson, JB and Fairall, CW (1998) Similarity relationships in the marine atmospheric surface layer for terms in the TKE and scalar variance budgets. *J. Atmos. Sci.*, 55:2311–2328

Elfouhaily, T, Chapron, B, Katsaros, K, and Vandemark, D (1997) A unified directional spectrum for long and short wind-driven waves. *J. Geophys. Res.*, 102:15781–15796

Hara, T and Belcher, SE (2002) Wind forcing in the equilibrium range of wind-wave spectra. *J. Fluid Mech.*, 470:223–245

Hara, T, Bock, EJ, and Lyzenga, D (1994) In situ measurements of capillary-gravity wave spectra using a scanning laser slope gauge and microwave radars. *J. Geophys. Res.*, 99:12593–12602

Hare, JE, Hara, T, Edson, JB, and Wilczak, JM (1997) A similarity analysis of the structure of airflow over surface waves. *J. Phys. Oceanogr.*, 27:1018–1037

Jähne, B and Riemer, JS (1990) Two dimensional wave number spectra of small-scale water surface waves. *J. Geophys. Res.*, 95:11531–11546

Janssen, PAEM (1989) Wind induced stress and the drag of air flow over sea waves. *J. Phys. Oceanogr.*, 19:745–754

Kitaigorodskii, SA (1973) *The physics of air-sea interaction*. Keter Press, Jerusalem, 9–73

Kondo, J (1975) Air-sea bulk transfer coefficients in diabatic conditions *Boundary-Layer Meteorol.*, 9:91–112

Kudyavtsev, VN and Makin, VK (2001) The impact of air-flow separation on the drag of the sea-surface. *Boundary-Layer Meteorol.*, 98:155–171

Kudyavtsev, VN and Makin, VK (2007) Aerodynamic roughness of the sea surface at high winds *Boundary-Layer Meteorol.*, doi:10.1007/s10546-007-9184-7

Kukulka, T and Hara, T (2005) Momentum flux budget analysis of wind-driven air-water interfaces. *J. Geophys. Res.*, 110:C12020

Large, WG and Pond, S (1981) Open ocean momentum flux measurements in moderate to strong winds. *J. Phys. Oceanogr.*, 11:324–336

Makin, VK (2005) A note on the drag of the sea surface at hurricane winds. *Boundary-Layer Meteorol.*, 115:169–176

Makin, VK and Kudryavtsev, VN (1999) Coupled sea surface-atmosphere model: 1. *J. Geophys. Res.*, 104:7613–7623

Makin, VK and Kudryavtsev, VN (2002) Impact of dominant waves on sea drag. *Boundary-Layer Meteorol.*, 103:83–99

Makin, VK, Kudyavtsev, VN, and Mastenbroek, C (1995) Drag of the sea surface. *Boundary-Layer Meteorol.*, 73:159–182

Melville, WK (1994) Energy dissipation by breaking waves. *J. Phys. Ocean.*, 24:2041–2049

Moon, IJ, Ginis, I, Hara, T, Belcher, SE, and Tolman, HL (2004) Effect of surface waves on air-sea momentum exchange. Part I: effect of mature and growing seas. *J. Atmos. Sci.*, 61:2321–2333

Phillips, OM (1985) Spectral and statistical properties of the equilibrium range in wind-generated gravity waves. *J. Fluid Mech.*, 156:505–531

Phillips, OM, Posner, FL, and Hansen, J P (2001) High range resolution radar measurements of the speed distribution of breaking events in wind-generated ocean waves: Surface impulse and wave energy dissipation rates. *J. Phys. Ocean*, 31:450-460

Plant, WJ (1982) A relationship between wind stress and wave slope. *J. Geophys. Res.*, 87:1961–1967

Powell, MD, Vickery, PJ, and Reinhold, TA (2003) Reduced drag coefficient for high wind speeds in tropical cyclones. *Nature*, 422:279–283

Reul, N (1998) Etude expérimentale de la structure de l'écoulement d'air au-dessus de vagues courtes déferlantes. *Dissertation*, 334 pp., Univ. de la Mediterranee, Marseille, France

Reul, N, Branger H, and Giovanangeli J–P (2007) Air flow structure over short-gravity breaking water waves. *Boundary-Layer Meteorol.*, 126, doi:10.1007/s10546-007-9240-3

Taylor, PK and Yelland, MJ (2000) On the apparent imbalance term in the turbulent kinetic energy budget. *J. Atmos. Ocean. Tech.*, 17:82–89

van Driest, ER (1956) On turbulent flow near a wall. *J. Aeronaut. Sci.*, 23:1007–1011

Wu, J (1983) Sea-surface drift currents induced by wind and waves. *J. Phys. Ocean.*, 13:1441–1451

Wu, CH and Yao A (2004) Laboratory measurements of limiting freak waves on currents *J. Geophys. Res., 109, C12002, doi:10.1029/2004JC002612*

Veron, F, G Saxena, and Misra SK (2007) Measurements of the viscous tangential stress in the airflow above wind waves *Geophys. Res. Lett., 34, L19603, doi:10.1029/2007GL031242*

Address for Offprints:
College of Marine and Earth Studies, University of Delaware
112C Robinson Hall
Newark, DE 19716, U.S.A.
email: jmueller@udel.edu; fveron@udel.edu
phone: (302)831-6658
fax: (302)831-6638